

Spin current generation in organic antiferromagnets

Makoto Naka^{1*}, Satoru Hayami², Hiroaki Kusunose³, Yuki Yanagi⁴, Yukitoshi Motome⁵, and Hitoshi Seo^{6,7}

¹Waseda Institute for Advanced Study, Waseda University, Shinjuku, Tokyo 169-8050, Japan

²Department of Physics, Hokkaido University, Sapporo, Hokkaido 060-0810, Japan

³Department of Physics, Meiji University, Kawasaki, Kanagawa 214-8571, Japan

⁴Institute for Materials Research, Tohoku University, Sendai, Miyagi 980-8577, Japan

⁵Department of Applied Physics, The University of Tokyo, Bunkyo, Tokyo 113-8656, Japan

⁶Condensed Matter Theory Laboratory, RIKEN, Wako, Saitama 351-0198, Japan and

⁷Center for Emergent Matter Science (CEMS), RIKEN, Wako, Saitama 351-0198, Japan

(Dated: February 8, 2019)

Spin current—a flow of electron spins without a charge current—is an ideal information carrier free from Joule heating for electronic devices. The celebrated spin Hall effect^{1,2}, which arises from the relativistic spin-orbit coupling, enables us to generate and detect spin currents in inorganic materials and semiconductors^{3–6}, taking advantage of their constituent heavy atoms. In contrast, organic materials consisting of molecules with light elements have been believed to be unsuited for spin current generation. Here we show that a class of organic antiferromagnets with checkerplate type molecular arrangements can serve as a spin current generator by applying a thermal gradient or an electric field, even with vanishing spin-orbit coupling. Our findings provide another route to create a spin current distinct from the conventional spin Hall effect and open a new field of spintronics based on organic magnets having advantages of small spin scattering and long lifetime.

Organic metals and semiconductors⁷ possess a variety of features not shared by inorganic materials, e.g., light, flexible, and toxic-element-free. They have been rapidly developed over the past decades for use in consumer electronic devices, such as organic transistors, light-emitting diodes, and piezo actuators. These accomplishments, in combination with recent evolutions of inorganic spintronics based on spin current physics, have promoted a new field, i.e., organic spintronics. Now significant efforts are being made to elucidate spin transport phenomena in organic semiconductors^{8–10}. However, organic spintronics devices are actually not purely organic but are hybrid with inorganic materials, because the generation of spin current basically requires an inorganic magnetic electrode. In fact, attempts for exploiting organic materials as the spin current generator are quite limited¹¹. Here, we theoretically propose a microscopic mechanism of spin current generation in organic materials utilizing an archetypal antiferromagnet.

κ -(BEDT-TTF)₂Cu[N(CN)₂]Cl (abbreviated as κ -Cl) is a well-studied organic insulator, showing a variety of cooperative phenomena, e.g., antiferromagnetic (AFM) ordering, insulator-to-metal transition, and superconductivity, at low temperatures and/or under pressures^{12–17}. The crystal structure is composed of an alternate stack-

ing of two dimensional conducting BEDT-TTF (abbreviated as ET) layers and insulating Cu[N(CN)₂]Cl layers. Figure 1a shows the molecular arrangement (called κ -type) in the conducting layer, where four ET molecules in the unit cell form two kinds of dimers with different orientations, termed *A* and *B*, connected by a glide operation (mirror and half translation).

This class of organic materials is known to show a simple electronic structure composed of “frontier” molecular orbitals^{18,19}. In the κ -type materials, the frontier orbitals in each ET dimer become strongly hybridized by the intra-dimer transfer integral shown in Fig. 1b, and constitute bonding and antibonding orbitals. They result in four bands as there are two dimers in the unit cell: two lower(higher)-energy bands are from the (anti-)bonding orbitals, as shown in Fig. 1c. The system has three electrons per two dimers on average, and hence, the four bands are three-quarter filled.

In the last few decades, extensive studies have been made for understanding the cooperative phenomena in this system^{20–22}. Most of them, however, are based on the single-band picture, where the two fully-occupied bands are disregarded (see the broken lines in Fig. 1c). This approach is justified in the large dimerization limit¹⁸, where the crystallographic distinction of the *A* and *B* dimers is lost. In other words, the glide symmetry in the molecular arrangement in the conducting layer is disregarded in the previous studies. In the following, we will discuss that the breaking of the glide symmetry by the AFM ordering plays an essential role in a peculiar spin current generation.

Results

We investigate electronic structures and spin current transport properties of κ -Cl based on the Hubbard model, taking into account the distinct two types of dimers and the anisotropy in the transfer integrals between them¹⁸, $(t_a, t_p, t_q, t_b) = (-0.207, -0.102, 0.043, -0.067)$ eV, evaluated by a first-principles calculation²³ (see Fig. 1b). At three-quarter filling where the number of electrons in the unit cell is equal to 6, the ground state exhibits a metal-to-insulator transition from a paramagnetic (PM) phase to an AFM phase on increasing the intra-molecular Coulomb interaction U ^{18,24}.

A crucial feature in the AFM state of κ -Cl is that up

and down spins are situated on the dimers with the different orientations as shown in Fig. 1b, resulting in the glide symmetry breaking with respect to the yz plane. Here we consider the glide operation not acting on the spins. The molecular orientation makes the AFM state not invariant under the combination of time reversal and spatial translation operations, unlike simple Néel-type AFM state, e.g., on the square lattice. This situation gives rise to an energy band splitting depending on the spins, which has been overlooked previously. Figure 1d shows the band structure in the AFM state, calculated within the self-consistent mean-field theory (see Methods). The spin splitting appears in the whole Brillouin zone except on the k_x -, k_y -axes and the zone boundary as shown in Fig. 1e.

The origin of the spin splitting is understood from the real-space anisotropy induced by the AFM ordering as follows. Figures 2a-2f show the effective inter-dimer transfer integrals between the antibonding orbitals, calculated by the second-order perturbation with respect to the inter-orbital hybridizations (see Methods). In the PM phase, as shown in Figs. 2a and 2b, the A and B dimers show different real-space anisotropies owing to the molecular orientations, but the anisotropies are symmetric with respect to the glide operation and do not depend on the spin degree of freedom. In the AFM phase, in contrast, the transfer integrals for up-spin electrons on the A dimer (Fig. 2c) and down-spin electrons on the B dimer (Fig. 2f) are enhanced, whereas their counterparts (Figs. 2d and 2e) are reduced. This spin-dependent anisotropy leads to the spin splitting.

The real-space anisotropies also show up in the effective spin exchange interactions in the Heisenberg model, derived from the above Hubbard model. Note that the system retains $SU(2)$ symmetry because of the absence of the spin-orbit coupling. Figure 3a shows the spatial distributions of the nearest-neighbor (NN) exchange interactions J and J' , and the next-nearest-neighbor (NNN) interactions K and K' . K and K' arise from fourth-order perturbation processes with respect to the NN transfer integrals (see Methods). As shown in Fig. 3b, K' becomes much smaller than K for realistic parameters. Then, the AFM magnon dispersion of the Heisenberg model exhibits a spin splitting as shown in Fig. 3c, where we take $K = 2$ meV and $K' = 0$ for simplicity, and $J = 80$ meV and $J' = 20$ meV¹³ (see Methods). Similar spin splitting was reported in non-centrosymmetric systems with the spin-orbit coupling^{25,26}, but the present mechanism requires neither non-centrosymmetry nor the spin-orbit coupling.

The spin-split magnon excitations lead to a spin current generation. Figure 3d shows the off-diagonal spin current conductivity, along the x -axis with respect to the thermal gradient along the y -axis, χ_{xy}^{SQ} , as a function of temperature T and the exchange interaction K , calculated by the linear response theory (see Methods). The range of T is chosen well below the Néel temperature of κ -Cl, 23 K. The polarization of the spin current

is parallel to the AFM moment, and the damping factor η is fixed at 1 meV. We obtain nonzero χ_{xy}^{SQ} for $T > 0$ and $K > 0$, which monotonically increases in proportion to T^2 and K . Remarkably, the conductivity tensor χ^{SQ} is symmetric, $\chi_{xy}^{\text{SQ}} = \chi_{yx}^{\text{SQ}}$, with vanishing diagonal elements, $\chi_{xx}^{\text{SQ}} = \chi_{yy}^{\text{SQ}} = 0$. This leads to peculiar field-angular dependence as shown in Fig. 3e, which is distinct from the conventional spin Nernst effect where the spin current is always perpendicular to the thermal gradient.

We find that χ_{xy}^{SQ} is inversely proportional to the damping factor η and diverges in the clean limit ($\eta = 0$), in analogy with the diagonal thermal conductivities κ_{xx} and κ_{yy} (see Supplementary Information). This indicates that the ratio $\alpha \equiv |2J\chi_{\mu\nu}^{\text{SQ}}/\hbar\kappa_{\nu\nu}|$, which is used in the literatures as the conversion rate from the heat current to the spin current, does not depend on η , however, depends on the field angle. Therefore, we choose $\mu = x$ and $\nu = y$ since κ_{yy} is largest in this direction, considering its implication as the conversion rate. Figure 3f shows K dependences of α at $k_B T = 0.5$ meV and 1 meV linearly increasing with K , but almost independent of T . The heat-spin current conversion efficiency reaches $\sim 5\%$ for the case of κ -Cl, which is close to one-quarter of that in Pt due to the strong spin-orbit coupling²⁷.

Now we propose another way of a spin current generation, in carrier doped metallic regions. The carrier doping has recently been realized experimentally^{16,17}. We here focus on the electron-doping case where the AFM metallic state is stable in our model. Figure 4a shows the off-diagonal spin current conductivity induced by the electric field, $\chi_{xy}^{\text{SC}} (= \chi_{yx}^{\text{SC}})$, as a function of the Coulomb interaction U and the number of electrons in the unit cell n in the ground state (see Methods). χ_{xy}^{SC} is zero in the PM metallic and the AFM insulating phases, while it turns finite in the AFM metallic phase where the Fermi energy lies in the top band in Fig. 1d, whose spin splitting was shown in Fig. 1e. We note that the sign of χ_{xy}^{SC} changes around $n = 6.2$, associated with the change in the Fermi surface topology as shown in the insets of Fig. 4a. This conductivity tensor is also symmetric with zero diagonal components and inversely proportional to the damping factor (see Supplementary Information). We define the charge-spin current conversion rate by $\beta \equiv |2e\chi_{yx}^{\text{SC}}/\hbar\sigma_{xx}|$, in analogy with α above (the electrical conductivity $\sigma_{\nu\nu}$ becomes largest in the $\nu = x$ direction due to the quasi-one-dimensional Fermi surfaces). As shown in Fig. 4b, in the lightly doped region with small σ_{xx} , β become relatively large and approaches 7 %, comparable to the spin Hall effect in Pt²⁸, while in the highly doped region, it decreases because of the suppression of the AFM ordering and the spin splitting.

Discussion

The present spin current generation is strikingly different from the conventional spin Nernst and Hall effects. In the conventional mechanisms, a spin current is activated by the spin-orbit coupling in non-centrosymmetric

lattice structures. The conductivity tensor is antisymmetric, namely, the generated spin current is always perpendicular to the applied field direction and the conversion rate is invariant under the rotation of the field. The transverse conductivity converges to a finite value in the clean limit because of the dominant inter-band contributions^{1,2}. However, the strong spin-orbit coupling also disturbs the spin polarization of carriers via the spin-flipping process.

In stark contrast, the present mechanism requires neither the spin-orbit coupling nor spatial inversion symmetry breaking. The spin current conductivity is described by the symmetric tensor, which diverges in the clean limit due to the intra-band contributions. In κ -type ET systems, the Dzyaloshinskii-Moriya interaction due to the spin-orbit coupling is estimated to be a few Kelvin^{14,29}, which is much smaller than the NNN exchange interaction K . Furthermore, the organic compounds have relatively less impurities. These facts ensure a long spin lifetime in κ -Cl, which facilitates the experimental detection. This phenomenon has a similarity with the spin current generation in ferromagnetic metals in the sense that the time reversal symmetry is lost, whereas the total magnetization is absent here. This has the advantage of small field leakage as discussed in AFM spintronics. These considerations lead us to conclude that our proposal provides a new type of spin current generation essentially distinct from the other existing mechanisms.

Molecular orientations in organic materials are essentially equivalent to long-range ordering of anisotropic electronic orbitals. Therefore, our new mechanism can be applied to other AFM materials with orbital ordering such as transition metal compounds including Jahn-Teller active elements. In this point of view, our finding strikes out a new direction of materials exploration for spintronics without relying on the spin-orbit coupling.

Methods

Mean-field approximation. The Hamiltonian of the Hubbard model on the κ -type lattice is given by

$$\begin{aligned} \mathcal{H}_{\text{Hubb}} = & U \sum_{i\mu} n_{i\mu\uparrow} n_{i\mu\downarrow} + t_a \sum_{i\sigma} (c_{ia\sigma}^\dagger c_{ib\sigma} + \text{H.c.}) \\ & + \sum_{\langle ij \rangle \mu \mu' \sigma} t_{ij}^{\mu \mu'} (c_{i\mu\sigma}^\dagger c_{j\mu'\sigma} + \text{H.c.}), \end{aligned} \quad (1)$$

where $c_{i\mu\sigma}$ and $n_{i\mu\sigma} (= c_{i\mu\sigma}^\dagger c_{i\mu\sigma})$ are the annihilation operator and the number operator of an electron with a spin $\sigma (= \uparrow, \downarrow)$, on the frontier orbital of molecular site $\mu (= a, b)$ in the i th dimer, respectively, U is the intra-molecular Coulomb interaction, and t_a and $t_{ij}^{\mu \mu'}$ are the inter-molecular transfer integrals shown in Fig. 1b. We treat the Coulomb interaction term within the mean-field approximation as $n_{i\mu\uparrow} n_{i\mu\downarrow} \simeq n_{i\mu\uparrow} \langle n_{i\mu\downarrow} \rangle + \langle n_{i\mu\uparrow} \rangle n_{i\mu\downarrow} - \langle n_{i\mu\uparrow} \rangle \langle n_{i\mu\downarrow} \rangle$, and determine the expectation values self-consistently so as to minimize the total energy of the system.

Effective electron transfer integrals. We divide the mean-field Hamiltonian in the AFM phase into three terms as $\mathcal{H}_{\text{MF}} = \mathcal{H}_{\text{intra}} + \mathcal{H}_{\text{inter}} + \mathcal{H}_{\text{AFM}}$, where the first and second terms represent the intra-orbital and inter-orbital transfer integrals, respectively, and the third term is the local AFM field. By taking the linear combinations of the original electron operators, we define the annihilation operator of an electron in the antibonding (bonding) orbital on the i th dimer as $\tilde{c}_{i\alpha(\beta)\sigma} = (c_{ia\sigma} - (+)c_{ib\sigma})/\sqrt{2}$, and the three terms are given by

$$\mathcal{H}_{\text{intra}} = t_a \sum_{i\sigma} (\tilde{n}_{i\beta\sigma} - \tilde{n}_{i\alpha\sigma}) + \sum_{\langle ij \rangle \nu \sigma} (\tau_{ij}^{\nu\nu} \tilde{c}_{i\nu\sigma}^\dagger \tilde{c}_{j\nu\sigma} + \text{H.c.}), \quad (2)$$

$$\mathcal{H}_{\text{inter}} = \sum_{\langle ij \rangle \nu \sigma} (\tau_{ij}^{\nu\bar{\nu}} \tilde{c}_{i\nu\sigma}^\dagger \tilde{c}_{j\bar{\nu}\sigma} + \text{H.c.}), \quad (3)$$

$$\mathcal{H}_{\text{AFM}} = \frac{U\delta}{4} \left(\sum_{i \in (B)\nu\sigma} - \sum_{i \in (A)\nu\sigma} \right) \sigma \tilde{n}_{i\nu\sigma}, \quad (4)$$

where the number operator is given by $\tilde{n}_{i\nu\sigma} = \tilde{c}_{i\nu\sigma}^\dagger \tilde{c}_{i\nu\sigma}$, and $\bar{\nu} = \beta$ (α) for $\nu = \alpha$ (β). The transfer integral between the neighboring dimers is given by $\tau_{ij} = \mathbf{U} t_{ij} \mathbf{U}^T$, by using the two-by-two unitary matrix \mathbf{U} satisfying $(\tilde{c}_{\alpha\sigma}, \tilde{c}_{\beta\sigma})^T = \mathbf{U} (c_{a\sigma}, c_{b\sigma})^T$. The amplitude of the local AFM field is given by $\delta = \langle \tilde{n}_{i \in A \uparrow} \rangle - \langle \tilde{n}_{i \in A \downarrow} \rangle = \langle \tilde{n}_{i \in B \downarrow} \rangle - \langle \tilde{n}_{i \in B \uparrow} \rangle$, where $\tilde{n}_{i\sigma} = \sum_{\nu} \tilde{n}_{i\nu\sigma}$.

We treat $\mathcal{H}_{\text{inter}}$ as the perturbation term and calculate the effective transfer integrals for the bonding and antibonding orbitals up to $\mathcal{O}(\mathcal{H}_{\text{inter}}^2)$. In the \mathbf{k} space, the mean-field Hamiltonian is described by the matrix form as $\mathcal{H}_{\text{MF}} = \sum_{\mathbf{k}\sigma} \psi_{\mathbf{k}\sigma}^\dagger (\mathbf{H}_{\mathbf{k}\sigma}^{(0)} + \mathbf{V}_{\mathbf{k}\sigma}) \psi_{\mathbf{k}\sigma}$, where $\mathbf{H}_{\mathbf{k}\sigma}^{(0)}$ and $\mathbf{V}_{\mathbf{k}\sigma}$ are the unperturbed and perturbed terms, respectively, given by 4×4 matrices. $\psi_{\mathbf{k}\sigma}$ is the vector of the annihilation operators of the Bloch states, which is chosen so as to diagonalize the unperturbed term as $\hat{H}_{\mathbf{k}\sigma}^{(0)} |\mathbf{k}\nu_\sigma^\xi\rangle = \varepsilon_{\mathbf{k}\nu\sigma}^\xi |\mathbf{k}\nu_\sigma^\xi\rangle$, where $\xi (= 1, 2)$ indicates the two bands in the bonding and antibonding bands each originating from the two dimers in the unit cell. The second-order perturbation term $\mathbf{H}_{\mathbf{k}\sigma}^{(2)}$ is decomposed into two 2×2 matrices for the antibonding (α) and bonding bands (β) as $\mathbf{H}_{\mathbf{k}\sigma}^{(2)} = \mathbf{h}_{\mathbf{k}\alpha\sigma}^{(2)} \oplus \mathbf{h}_{\mathbf{k}\beta\sigma}^{(2)}$. The matrix element of $\mathbf{h}_{\mathbf{k}\nu\sigma}^{(2)}$ is given by

$$h_{\nu;\xi\xi'}^{(2)} = \sum_{\eta=1,2} \frac{\langle \nu^\xi | \hat{V} | \bar{\nu}^\eta \rangle \langle \bar{\nu}^\eta | \hat{V} | \nu^{\xi'} \rangle}{\varepsilon_{\bar{\nu}}^\eta - \varepsilon_\nu^\eta}, \quad (5)$$

where the indices \mathbf{k} and σ are omitted for simplicity. By the Fourier transformation of $\mathbf{H}_{\mathbf{k}\sigma}^{(2)}$, we obtain the effective transfer integrals shown in Fig. 2.

Next-nearest-neighbor exchange interactions. From the Hubbard model in equation (1), we derive the effective NNN exchange interaction in the restricted space where each antibonding orbital is occupied by one

hole due to the strong Coulomb interaction U . The NNN exchange interaction is derived from the fourth-order perturbation process with respect to the inter-dimer transfer integrals, which is given by

$$\mathcal{H}^{(4)} = \mathcal{P}\mathcal{V}\left(\frac{1}{E_I - \mathcal{H}^{(0)}}\mathcal{Q}\mathcal{V}\right)^3 |I\rangle\langle I|, \quad (6)$$

where \mathcal{P} and \mathcal{Q} are the projection operators onto inside and outside of the restricted space, respectively, and satisfy $\mathcal{P} + \mathcal{Q} = 1$, \mathcal{V} is the perturbation given by the third term in equation (1), $\mathcal{H}^{(0)}$ is the unperturbed Hamiltonian given by the first and second terms in equation (1), and E_I is the energy of the initial eigenstate $|I\rangle$ of $\mathcal{H}^{(0)}$. The resultant exchange interaction on the NNN bond between the A dimers denoted by K in the middle panel of Fig. 3a is given by

$$\mathcal{H}_{ijk} = \tilde{J}\left(\mathbf{S}_i \cdot \mathbf{S}_j + \mathbf{S}_j \cdot \mathbf{S}_k - \frac{1}{2}\right) + K\left(\mathbf{S}_i \cdot \mathbf{S}_k - \frac{1}{4}\right), \quad (7)$$

where the indices ijk denote the three neighboring dimers, \mathbf{S}_i is the spin operator of the i th dimer, and K is the NNN exchange constant. \tilde{J} is the NN exchange constant arising from the fourth-order perturbation process, which does not contribute to the magnon splitting. The details of the fourth-order process and the explicit form of K (and K') are given in Supplementary Information.

Linear spin wave approximation. The effective Heisenberg model involving the NNN exchange interaction is given by

$$\begin{aligned} \mathcal{H}_{\text{Heis}} = & J \sum_{\langle ij \rangle} \mathbf{S}_i \cdot \mathbf{S}_j + J' \sum_{\langle ij \rangle'} \mathbf{S}_i \cdot \mathbf{S}_j \\ & + K \sum_{\langle\langle ij \rangle\rangle} \mathbf{S}_i \cdot \mathbf{S}_j + K' \sum_{\langle\langle ij \rangle\rangle'} \mathbf{S}_i \cdot \mathbf{S}_j, \end{aligned} \quad (8)$$

where $\langle ij \rangle$ and $\langle ij \rangle'$ stand for the diagonal and horizontal NN bonds on the equilateral triangular lattice, $\langle\langle ij \rangle\rangle$ and $\langle\langle ij \rangle\rangle'$ are the NNN bonds shown in Fig. 3a. By using the Holstein-Primakoff transformation, we obtain the linear spin-wave Hamiltonian given by

$$\begin{aligned} \mathcal{H}_{\text{Heis}} \simeq \mathcal{H}_{\text{LSW}} = & \frac{1}{2} \sum_{\mathbf{k}} [A_{\mathbf{k}} a_{\mathbf{k}}^\dagger a_{\mathbf{k}} + B_{\mathbf{k}} b_{-\mathbf{k}}^\dagger b_{-\mathbf{k}} \\ & + C_{\mathbf{k}} (a_{\mathbf{k}}^\dagger b_{-\mathbf{k}}^\dagger + a_{\mathbf{k}} b_{-\mathbf{k}})], \end{aligned} \quad (9)$$

where $a_{\mathbf{k}}$ and $b_{\mathbf{k}}$ are the Fourier transforms of the annihilation operators of magnons on the A and B dimers, respectively. The coefficients are given by

$$\begin{aligned} A_{\mathbf{k}} = & 4J + 2J'[\cos(\mathbf{k} \cdot \mathbf{a}_x) - 1] \\ & + 2K[\cos(\mathbf{k} \cdot (\mathbf{a}_x + \mathbf{a}_y)) - 1] \\ & + 2K'[\cos(\mathbf{k} \cdot (\mathbf{a}_x - \mathbf{a}_y)) - 1], \end{aligned} \quad (10)$$

$$\begin{aligned} B_{\mathbf{k}} = & 4J + 2J'[\cos(\mathbf{k} \cdot \mathbf{a}_x) - 1] \\ & + 2K[\cos(\mathbf{k} \cdot (\mathbf{a}_x - \mathbf{a}_y)) - 1] \\ & + 2K'[\cos(\mathbf{k} \cdot (\mathbf{a}_x + \mathbf{a}_y)) - 1], \end{aligned} \quad (11)$$

and

$$\begin{aligned} C_{\mathbf{k}} = & 2J[\cos(\mathbf{k} \cdot (\mathbf{a}_x + \mathbf{a}_y)/2) \\ & + \cos(\mathbf{k} \cdot (\mathbf{a}_x - \mathbf{a}_y)/2)], \end{aligned} \quad (12)$$

where \mathbf{a}_x and \mathbf{a}_y are the primitive translational vectors. \mathcal{H}_{LSW} is easily diagonalized by the standard Bogoliubov transformation, and the magnon energy dispersion shown in Fig. 3e is obtained.

Spin current conductivity to a thermal gradient. The spin current and energy current operators in the magnon system³⁰ are given by

$$\mathbf{J}_{S^z} = \frac{1}{i\hbar} [\mathbf{P}_{S^z}, \mathcal{H}_{\text{LSW}}] \quad (13)$$

and

$$\mathbf{J}_E = \frac{1}{i\hbar} [\mathbf{P}_E, \mathcal{H}_{\text{LSW}}], \quad (14)$$

respectively. \mathbf{P}_{S^z} and \mathbf{P}_E are the spin polarization and the energy polarization operators defined by $\mathbf{P}_{S^z} = \hbar \sum_i S_i^z \mathbf{R}_i$ and $\mathbf{P} = \sum_i \mathcal{H}_i \mathbf{R}_i$, respectively, where \mathbf{R}_i is the position vector of the center of the i th dimer and \mathcal{H}_i is the local energy density defined by $\mathcal{H}_{\text{LSW}} = \sum_i \mathcal{H}_i$, by the Fourier transformation of equation (9). In the magnon system where the chemical potential is zero, the heat current operator \mathbf{J}_Q is identical to the energy current operator \mathbf{J}_E . We note that the spin is a conserved quantity and the spin current is well defined here since our model does not include the spin-orbit coupling. In the linear response theory, the spin current conductivity to a static thermal gradient is given by

$$T\chi_{\mu\nu}^{\text{SQ}} = \lim_{\omega \rightarrow 0} \frac{Q_{\mu\nu}^{\text{SQ}}(\omega) - Q_{\mu\nu}^{\text{SQ}}(0)}{i\omega}, \quad (15)$$

where μ and ν represent the spatial axes x and y . The spin-current-heat-current response function $Q_{\mu\nu}^{\text{SQ}}(\omega)$ is given by the Kubo formula

$$Q_{\mu\nu}^{\text{SQ}}(\omega) = \frac{i}{\hbar V} \int_0^\infty dt e^{it(\omega + i\eta)} \langle [J_{S^z}^\mu(t), J_Q^\nu] \rangle_{\text{eq}}, \quad (16)$$

where $\mathbf{J}_{S^z}(t)$ is the Heisenberg representation of the spin current operator, η is the damping factor, V is the volume of the system, and $\langle \cdots \rangle_{\text{eq}}$ represents the thermal average under the temperature T .

Spin current conductivity to an electric field. The spin current and charge current operators are defined by

$$\mathbf{J}_{S^z} = \frac{1}{i\hbar} [\mathbf{P}_{S^z}, \mathcal{H}_{\text{MF}}] \quad (17)$$

and

$$\mathbf{J} = \frac{1}{i\hbar}[\mathbf{P}, \mathcal{H}_{\text{MF}}], \quad (18)$$

respectively. \mathbf{P}_{sz} and \mathbf{P} are the spin s^z polarization and the electric polarization operators defined by $\mathbf{P}_{sz} = \hbar \sum_i s_i^z \mathbf{r}_i$ and $\mathbf{P} = -e \sum_i \mathbf{r}_i$, respectively, where $s_i^z = \frac{n_{i\uparrow} - n_{i\downarrow}}{2}$ is the spin operator of the i th molecule at the position vector \mathbf{r}_i . The spin current conductivity to an static electric field is given by

$$\chi_{\mu\nu}^{\text{SC}} = \lim_{\omega \rightarrow 0} \frac{Q_{\mu\nu}^{\text{SC}}(\omega) - Q_{\mu\nu}^{\text{SC}}(0)}{i\omega}. \quad (19)$$

The spin-current-charge-current response function $Q_{\mu\nu}^{\text{SC}}(\omega)$ is given by the Kubo formula

$$Q_{\mu\nu}^{\text{SC}}(\omega) = \frac{i}{\hbar V} \int_0^\infty dt e^{it(\omega + i\gamma)} \langle [J_{sz}^\mu(t), J^\nu] \rangle_0, \quad (20)$$

where $\mathbf{J}_{sz}(t)$ is the Heisenberg representation of the spin current operator, γ is the damping factor, and $\langle \dots \rangle_0$ represents the average with respect to the ground state.

-
- ¹ Murakami, S., Nagaosa, N., and Zhang, S. C. Dissipationless Quantum Spin Current at Room Temperature. *Science* **301**, 1348-1358 (2003).
 - ² Sinova, J., *et al.* Universal Intrinsic Spin Hall Effect. *Phys. Rev. Lett.* **92**, 126603 (2004).
 - ³ Kato, Y. K., Mayers, R. C., Gossard, A. C., and Awschalom, D. D. Observation of the Spin Hall Effect in Semiconductors. *Science* **306**, 1910-1913 (2004).
 - ⁴ Wunderlich, J., Kaestner, B., Sinova, J., and Jungwirth, T. Experimental Observation of the Spin-Hall Effect in a Two-Dimensional Spin-Orbit Coupled Semiconductor System. *Phys. Rev. Lett.* **94**, 047204 (2005).
 - ⁵ Saitoh, E., Ueda, M., Miyajima, H., and Tatara, G. Conversion of spin current into charge current at room temperature: Inverse spin-Hall effect. *Appl. Phys. Lett.* **88**, 182509 (2006).
 - ⁶ Valenzuela, S. O. and Tinkham, M. Direct electronic measurement of the spin Hall effect. *Nature* **442**, 176-179 (2006).
 - ⁷ Homes, R., Bruetting, W., and Adachi, C. (eds) *Physics of Organic Semiconductors* (Wiley, 2012).
 - ⁸ Xiong, Z. H., Wu, D., Vardeny, V. Z., and Shi, J. Giant magnetoresistance in organic spin valves. *Nature* **427** 821-824 (2004).
 - ⁹ Szulcowski, G., Sanvito, S., and Coey, M. A spin of their own. *Nature Mater.* **8**, 693-695 (2009).
 - ¹⁰ Dediu, V. A., Luis, E. H., Bergenti, L., and Taliani, C. Spin routes in organic semiconductors. *Nature Mater.* **8**, 706-716 (2009).
 - ¹¹ Ando, K., Watanabe, S., Mooser, S., Saitoh, E., and Sirringhaus, H. Solution-processed organic spin-charge converter. *Nature Mater.* **12** 622-627 (2013).
 - ¹² Williams, J. M. *et al.* From semiconductor-semiconductor transition (42 K) to the highest- T_c organic superconductor, κ -(ET)₂Cu[N(CN)₂]Cl ($T_c = 12.5$ K). *Inorg. Chem.* **29**, 3272 (1990).
 - ¹³ Miyagawa, K., Kanoda, K., and Kawamoto, A. NMR Studies on Two-Dimensional Molecular Conductors and Superconductors: Mott Transition in κ -(BEDT-TTF)₂X. *Chem. Rev.* **104** 5625-5653 (2004).
 - ¹⁴ Ishikawa, R. *et al.* Zero-Field Spin Structure and Spin Reorientations in Layered Organic Antiferromagnet, κ -(BEDT-TTF)₂Cu[N(CN)₂]Cl. *J. Phys. Soc. Jpn.* **87** 064701 (2018).
 - ¹⁵ Kagawa, F., Miyagawa, K., and Kanoda, K. Unconventional critical behavior in a quasi-two-dimensional organic conductor. *Nature* **436**, 534-537 (2005).
 - ¹⁶ Kawasugi, Y. *et al.* Electron-hole doping asymmetry of Fermi surface reconstructed in a simple Mott insulator. *Nature Commun.* **7**, 12356 (2016).
 - ¹⁷ Oike, H., Miyagawa, K., Taniguchi, H., and Kanoda, K. Pressure-Induced Mott Transition in an Organic Superconductor with a Finite Doping Level. *Phys. Rev. Lett.* **114**, 067002 (2015).
 - ¹⁸ Kino, H. and Fukuyama, H. Phase diagram of two-dimensional organic conductors: (BEDT-TTF)₂X. *J. Phys. Soc. Jpn.* **65**, 2158-2169 (1996).
 - ¹⁹ Seo, H., Hotta, C., and Fukuyama, H. Toward Systematic Understanding of Diversity of Electronic Properties in Low-Dimensional Molecular Solids. *Chem. Rev.* **104** 5005-5036 (2004).
 - ²⁰ Morita, H., Watanabe, S., and Imada, M. Nonmagnetic insulating state near the Mott transition on lattices with geometrical frustration and implications for κ -(ET)₂Cu₂(CN)₃. *J. Phys. Soc. Jpn.* **71** 2109-2112 (2002).
 - ²¹ Mott Transition, Antiferromagnetism, and d -wave superconductivity in Two-Dimensional Organic Conductors. Kyung, B., and Tremblay, A.-M. S. *Phys. Rev. Lett.* **97**, 046402 (2006).
 - ²² Naka, M. and Ishihara, S. Electronic Ferroelectricity in a Dimer Mott insulator. *J. Phys. Soc. Jpn.* **79** 063707 (2010).
 - ²³ Koretsune, T. and Hotta, C. Evaluating model parameters of the κ - and β' -type Mott insulating organic solids. *Phys. Rev. B* **89**, 045102 (2014).
 - ²⁴ Watanabe, H., Seo, H., Yunoki, S. Phase Competition and Superconductivity in κ -(BEDT-TTF)₂X: Importance of Intermolecular Coulomb Interactions. *J. Phys. Soc. Jpn.* **86** 104705 (2016).
 - ²⁵ Iguchi, Y., Uemura, S., Ueno, K., and Onose, Y. Non-reciprocal magnon propagation in a noncentrosymmetric ferromagnet LiFe₅O₈. *Phys. Rev. B* **92**, 184419 (2015).
 - ²⁶ Hayami, S., Kusunose, H., and Motome, Y. Asymmetric Magnon Excitation by Spontaneous Toroidal Ordering. *J. Phys. Soc. Jpn.* **85**, 053705 (2016).
 - ²⁷ Meyer, S. *et al.* Observation of the spin Nernst effect. *Nature Mater.* **16**, 977-981 (2017).
 - ²⁸ Wang, Y., Deorani, P., Qiu, X., Kwon, J. H., and Yang, H., Determination of intrinsic spin Hall angle in Pt. *Appl. Phys. Lett.* **105**, 152412 (2014).
 - ²⁹ Winter, S. M., Riedl, K., and Valenti, R. Importance of

spin-orbit coupling in layered organic salts. *Phys. Rev. B* **95**, 060404(R) (2017).

- ³⁰ Katsura, H., Nagaosa, N., and Lee, P. A. Theory of the Thermal Hall Effect in Quantum Magnets. *Phys. Rev. Lett* **104**, 066403 (2010).

Acknowledgments

This work is supported by Grant-in-Aid for Scientific Research, No. JP16K17731, No. JP18H04296 (J-Physics), No. JP18K13488, No. JP15H05885 (J-Physics), No. JP26400377, and No. JP16H02393 from MEXT (Japan).

Author contributions

All authors contributed to conception, execution and write-up this project. The numerical and analytical calculations were performed by M.N.

Correspondence

Correspondence may be addressed to M.N.

Competing financial interests

The authors declare no competing financial interests.

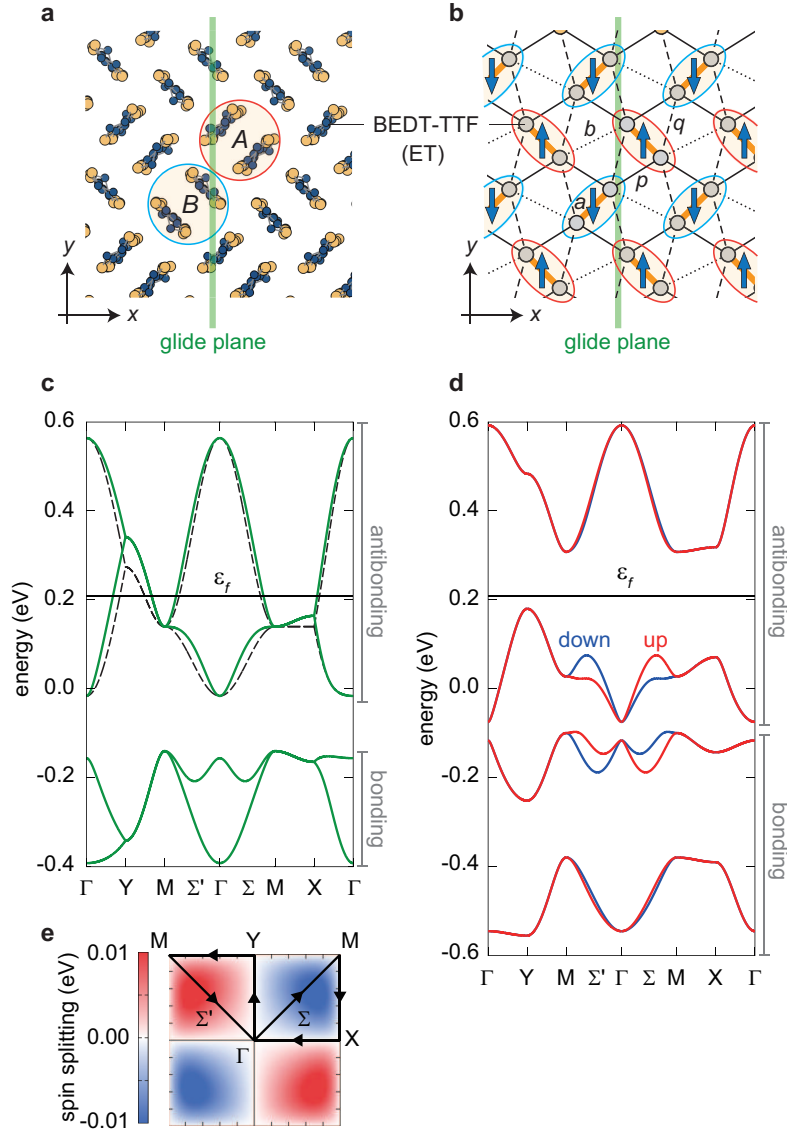


FIG. 1. **Schematic illustration of the lattice structure of κ -Cl and the energy bands.** **a**, Molecular arrangement in the two-dimensional conducting layer. The red and blue circles represent the two kinds of ET dimers, termed *A* and *B*, respectively, in the unit cell. The green line denotes the glide plane perpendicular to the xy plane. **b**, Network of the dominant electron transfer bonds, *a* (orange bold line), *b* (dotted line), *p* (solid line), and *q* (broken line). The gray circles represent the ET molecules, and the red and blue ellipses show the *A* and *B* dimers, respectively. The arrows represent the local spin moments in the AFM phase. We note that another glide plane exists when considering the layer stacking, but it does not affect our discussions. **c**, Energy band dispersion composed of the frontier orbitals of ET molecules in the PM metallic phase with the transfer integrals $(t_a, t_p, t_q, t_b) = (-0.207, -0.102, 0.043, -0.067)$ eV (green solid line) and that of the single-band picture in the large dimerization limit (broken line). The average electron number in the unit cell is 6 and the Fermi energy ε_f is shown. **d**, Energy band dispersion in the AFM insulating phase with the intra-molecular Coulomb interaction $U = 1$ eV, within the self-consistent mean-field theory. **e**, Contour map of the spin splitting subtracting the down-spin energy from the up-spin energy of the top band in **d** in the first Brillouin zone. The trajectory shows the symmetric lines in **c** and **d**.

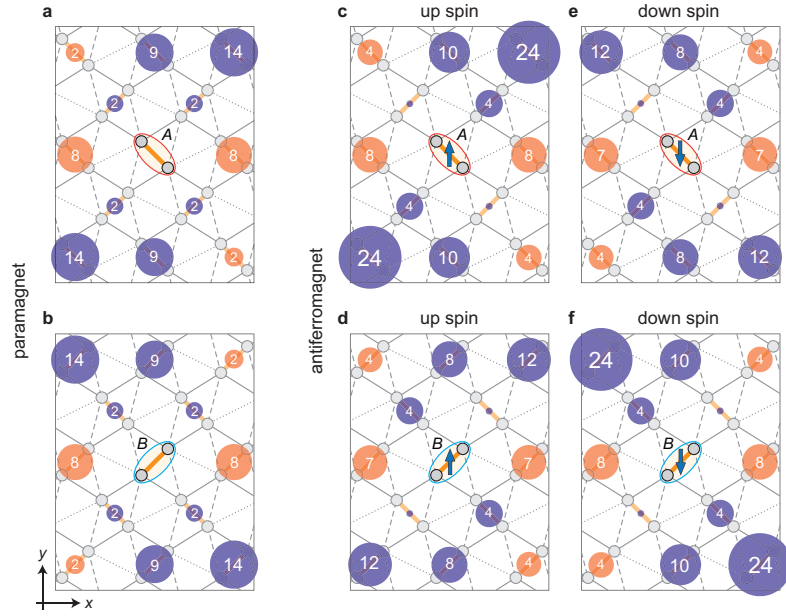


FIG. 2. **Spatial anisotropy of inter-dimer transfer integrals.** **a,b**, Effective transfer integrals between the central dimer (A in **a** and B in **b**) and the surrounding ones, obtained from the second-order perturbation processes with respect to the bonding-antibonding orbital hybridizations, in the PM phase. **c-f**, Effective transfer integrals calculated likewise for up- (**c,d**) and down-spin (**e,f**) electrons in the AFM phase (the local magnetic moment is about $0.168\hbar$). The areas of the red (blue) shaded circles represent the amplitudes of positive (negative) transfer integrals. The amplitudes are shown in the circles in unit of meV.

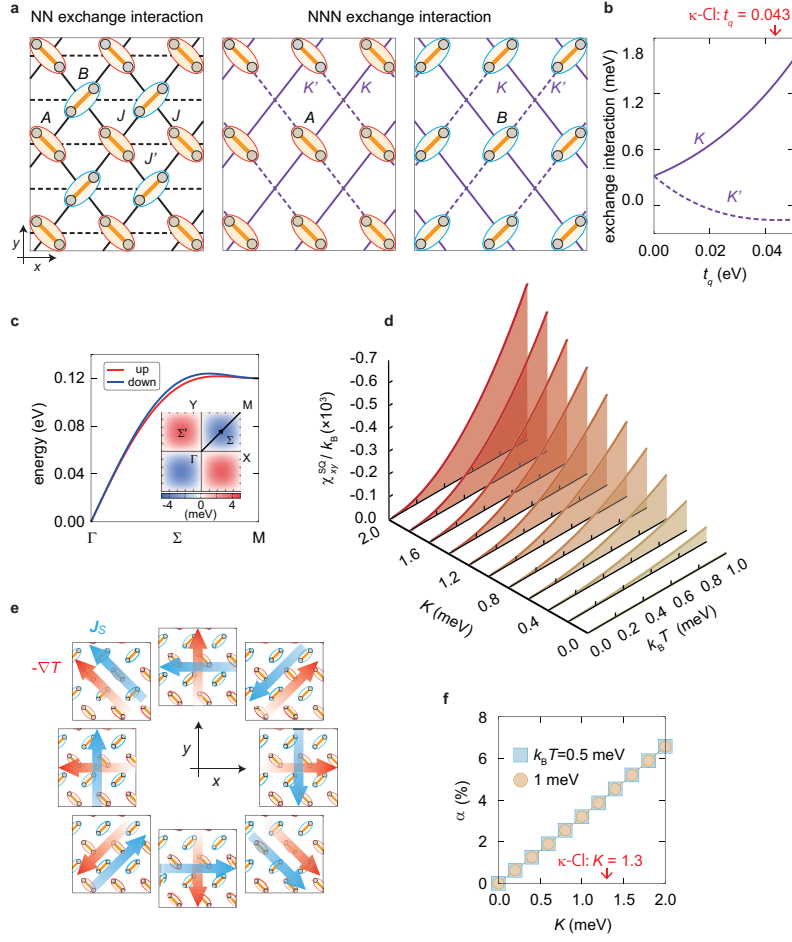


FIG. 3. Effective NNN exchange interactions, magnon dispersions, and heat-spin current conversion in the AFM insulating state. **a**, Real-space distribution of the NN exchange interactions J (solid lines) and J' (broken lines) between A and B dimers (left panel) and those of the NNN exchange interactions K (purple solid lines) and K' (purple broken lines) between A dimers (middle panel) and B dimers (right panel). **b**, t_q dependences of K and K' at $U = 1$ eV. The red arrow represents the value of t_q in κ -Cl. **c**, Magnon dispersions at $(J, J', K, K') = (80, 20, 2, 0)$ meV within the linear spin-wave theory. The inset shows a contour map of the spin splitting between the up- and down-spin magnons in the first Brillouin zone. **d**, (T, K) dependences of the spin current conductivity under a thermal gradient, χ_{xy}^{SQ} . The other exchange interactions and the damping factor are $(J, J', K', \eta) = (80, 20, 0, 1)$ meV. **e**, Illustrations of the field-angular dependence of the spin current generation. **f**, K dependences of the heat-spin current conversion rate $\alpha (= |2J\chi_{xy}^{SQ}/\hbar\kappa_{yy}|)$ at $k_B T = 0.5$ meV and 1 meV, where κ_{yy} is the thermal conductivity along the y -axis. The red arrow represents the value of K in κ -Cl.

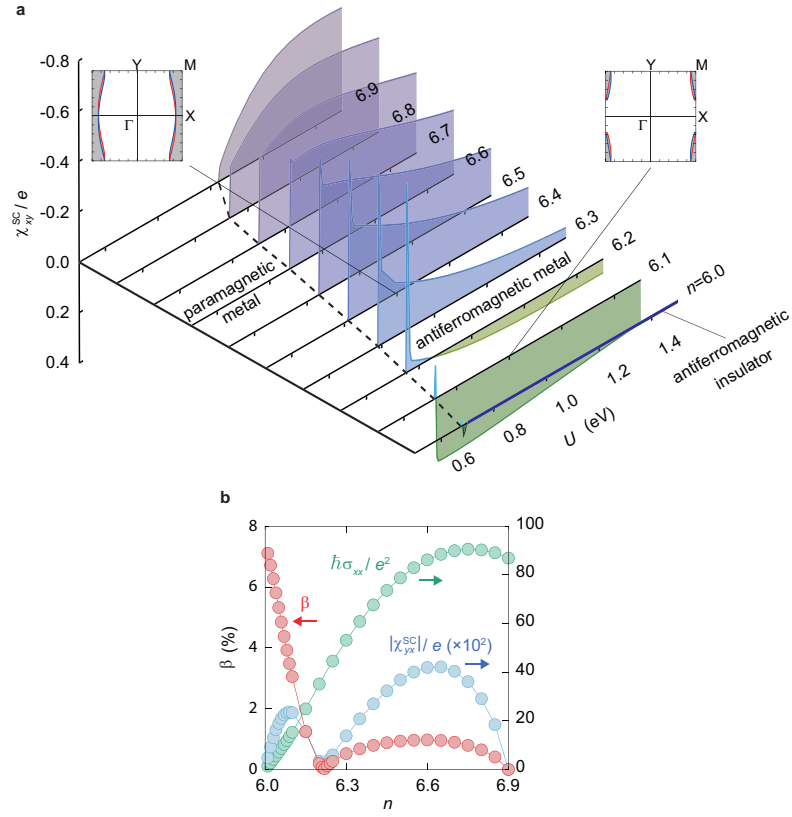


FIG. 4. **Charge-spin current conversion in the electron-doped AFM metallic state.** **a**, (U, n) dependences of the spin current conductivity to an electric field, χ_{xy}^{SC} . The broken line represents the phase boundary between the PM and AFM metallic phases, and the blue thick line shows the AFM insulating phase at three-quarter filling. The damping factor is $\gamma = 1$ meV. The insets show the Fermi surface structures of up-spin (red) and down-spin (blue) electrons at $(U, n) = (1 \text{ eV}, 6.1)$ and $(1 \text{ eV}, 6.4)$. The gray shaded areas denote the occupied states. **b**, n dependences of the charge-spin current conversion rate $\beta (= |2e\chi_{yx}^{SC}/\hbar\sigma_{xx}|)$, $|\chi_{yx}^{SC}|$, and the diagonal electrical conductivity σ_{xx} at $U = 1 \text{ eV}$.